

Effects of diameter polydispersity and small-range interactions on the structure of biocompatible colloidal nanoparticles

Aimê Gomes da Mata Kanzaki^a, Tiago de Sousa Araújo Cassiano^a, João Valeriano^b, Fabio Luis de Oliveira Paula^a, Leonardo Luiz e Castro^a

^aUniversidade de Brasília, Instituto de Física, Campus Universitário Darcy Ribeiro, Brasília, 70.910-900, DF, BR

^bAix-Marseille Université, CINAM, Turing Centre for Living Systems, Marseille, FR

Abstract

The particles of synthetic colloids are usually treated with chemical techniques to prevent the loss of colloidal stability caused by van der Waals and magnetic dipolar attractive interactions. However, understanding the counterbalance between the attractive and repulsive interactions is challenging due to the limitations of the conventional mesoscopic models at short nanoparticle separations. In this study, we examined three models that describe short-range interactions by proposing different corrections to the van der Waals energy for short distances. The three models show only a minimal deviation from energy extensivity, as expected of a system with a comparatively short interaction range. Our analysis shows that a more detailed microscopic model at short-range separations is crucial for proper sampling, which is necessary to estimate physical quantities adequately. The same model predicts that polydispersity can lead to an overall decrease in mean particle distance for a configuration with 5% colloidal volume fraction. The other, simpler models make the opposite prediction, which opens an interesting venue for experimental exploration that could shed light on the validity of this model. The predicted decrease in particle distance could lead to coagulation, suggesting a preference for ferrofluids with more uniform particle sizes, leading to lower attraction, but still responding to applied fields, as needed in most applications.

Keywords: Colloid, Ferrofluid, van der Waals, Cohesion energy, Born-Mayer repulsion, Extensivity, Monte Carlo

1. Introduction

Colloids, alongside their ample occurrence in nature and everyday products, are routinely synthesized in new varieties aiming at multiple applications. In particular, ferrofluids (magnetic colloids), made of magnetic iron oxide nanoparticles, have garnered significant interest due to their role in novel technological, biomedical, and environmental applications [1, 2, 3, 4]. Examples include their use as contrast agents in magnetic resonance imaging [5, 6], as multifunctional agents in theranostics [7], as a vehicle for the administration of targeted drugs [8, 9], and in cancer treatments through magnetohyperthermia [10, 11, 12, 13, 14, 15]. Improved targeted therapies, accurate diagnoses, and other innovative biomedical devices can emerge by combining the magnetic response of ferrofluids with the tailored functionalization of nanoparticle surfaces, thereby opening new frontiers in the field of nanomedicine.

A major issue in nanotechnological biomedicine [16] is the biocompatibility of the synthetic materials, being necessary to carry out extensive studies of their properties and functionalities to ensure that they are pharmacologically inert for incorporation into living systems. Ferrofluid-based biomedical applications impose strong constraints for practical use. Firstly, the particles must be chemically atoxic. Moreover, the field's magnitude and frequency must not be unrestrictedly high; otherwise, the application can harm the body. Another concern is that the attraction between the nanoparticles does not cause aggregation or floccu-

lation to an extent that damages the physiological medium into which they are inserted.

Computational simulation methods, such as molecular dynamics and Monte Carlo methods, have been used extensively to evaluate the effect of nanoparticle interactions on the ferrofluid properties [17], considering factors such as concentration [18], pH [19], ionic strength [20], surface charge [21], particle size [22], polymer architecture [23], external magnetic field [24, 25], and confinement (e.g. inside liposomes) [26]. Colloidal stability is determined through the energy balance between the attractive and repulsive forces acting on nanoparticles. Therefore, modifications to particle properties, such as surface functionalization or the addition of surfactants, can also alter the interaction energy between the particles and thus the colloidal stability of the ferrofluid. The DLVO theory [27] is frequently adapted to describe interactions in functionalized ferrofluids, considering effects such as surface functionalization and steric interference in interactions between particles or even in a mixed particles [28, 29]. These approaches are fundamental to formulating strategies that optimize the stability and functionality of ferrofluids.

However, the DLVO theory has its limitations. In the small-separation regime, the van der Waals interaction can diverge if not properly controlled, leading to nonphysical trapping regions in theoretical simulations. When two nanoparticles come too close, they snap together and become inseparable, forming an unrealistically strong binding. Consequently, this limitation leads to a poor description of agglomeration and complex formation. The conventional workaround is to implement a cutoff distance. Then, two neighboring nanoparticles closer than this limit have the same attractive energy. However, this approach also has its own flaws,

Correspondence: joao-pedro.valeriano-miranda@univ-amu.fr
(João Valeriano)

as the threshold distance is an arbitrary parameter and may still enforce trapping regions. In this context, developing improved strategies is crucial for both theoretical and practical perspectives. A better formalism of colloids for small-separation regimes might deliver a better description of agglomeration mechanisms, potentially offering better insights into how to mitigate them.

This work was mainly focused on the influence of size dispersion and short-range interaction on the self-organization of nanoparticles in magnetic colloids. We compared the results of three interparticle interaction models, differing mostly in their short-distance descriptions, used in Monte Carlo simulations of this reference system. We took as our study case a system formed by a magnetic fluid based on tartrate-coated magnetite nanoparticles [30] that was synthesized by thermal coprecipitation and dispersion method at $pH \sim 7$ under physiological conditions. The particle diameters were fitted into a log-normal distributed with modal diameter $D_0 = 7.17$ nm and dispersion $\sigma = 0.24$ (for the sake of comparison, we simulated the system with and without diameter polydispersity).

In Section 2 we introduce the three models, proposing different solutions for correcting the small-distance interaction energy. In Section 3 we describe the simulation methods for studying the ferrofluid system, and proceed with an analysis of the energy extensivity properties of the different models, having in mind that the finite range interactions could lead to nonlinear scaling of energy with system size. We proceed with the presentation of our main results in Section 4 followed by a final discussion and conclusion.

2. Models

Colloids are commonly modeled as an ensemble of N interacting nanoparticles in a dispersion medium. The balance between the particle interactions and eventual external agents dictates the macroscopic properties. In our case, the physical description of a colloid involves summing the van der Waals (U_{vdw}), electric (U_{edl}), steric (U_{ste}), and magnetic interactions (U_{mag}).

$$U = U_{vdw} + U_{edl} + U_{ste} + U_{mag}. \quad (1)$$

The three interaction models between the nanocolloidal particles differ in how the van der Waals and the electronic repulsion (EDL) interactions are described. All other interactions pertaining to the description of the ferrofluid remain the same regardless of the model.

First, consider the interactions that are common to all models. Let R_i and R_j be the radii of nanoparticles i and j positioned at \vec{r}_i and \vec{r}_j , respectively. Then, $r_{ij} \equiv |\vec{r}_i - \vec{r}_j|$ is the corresponding center-to-center distance as illustrated in Figure 1. The magnetic moment of the i -th nanoparticle is

$$\vec{m}_i = MV_{mag(i)}\hat{u}_i, \quad (2)$$

where \hat{u}_i is the unit vector along the direction of the magnetic moment of the nanoparticle, M is the magnetization of the magnetite, and $V_{mag(i)}$ is the ‘‘magnetic volume’’ of the nanoparticle, given by

$$V_{mag(i)} = \frac{4\pi}{3}(R_i - \delta_s)^3, \quad (3)$$

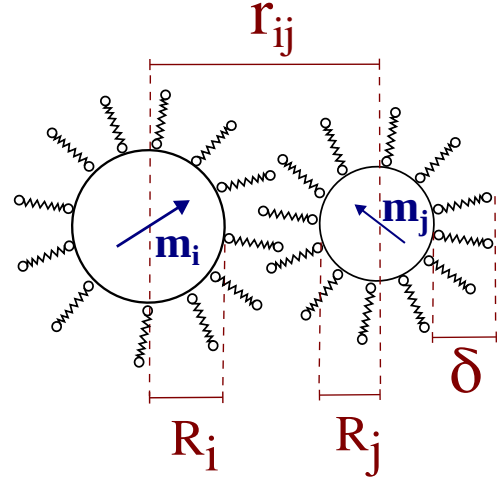


Figure 1: Illustration of pair of colloidal magnetic nanoparticles coated with surfactant molecules.

in which δ_s is the length of its non-magnetic shell. Therefore, the dipolar interaction energy between the nanoparticles is expressed as

$$U_{mag}(r_{ij}, \vec{m}_i, \vec{m}_j) = \frac{\mu}{4\pi} \left[\frac{\vec{m}_i \cdot \vec{m}_j - 3(\vec{m}_i \cdot \hat{r}_{ij})(\vec{m}_j \cdot \hat{r}_{ij})}{r_{ij}^3} \right], \quad (4)$$

where μ is the magnetic permeability of the solvent.

The steric repulsion energy reads [31]

$$U_{ste}(r_{ij}) = \begin{cases} \frac{\pi\xi k_B T}{2} (2R_i)(2R_j) \left[2 - \frac{(r_{ij}-2R_{ij})}{\delta} - \frac{r_{ij}}{\delta} \ln \left(\frac{2(R_{ij}+\delta)}{r_{ij}} \right) \right] & \text{for } r_{ij} < 2(R_{ij} + \delta), \\ 0 & \text{otherwise,} \end{cases} \quad (5)$$

in which ξ is the grafting parameter (surface density of the adsorbed molecules), δ is the length of the surfactant layers, and R_{ij} is the arithmetic mean of R_i and R_j ,

$$R_{ij} = \frac{R_i + R_j}{2}. \quad (6)$$

Let us now describe the interactions that differ across the models. The first model avoids the van der Waals divergence by limiting the separation distance to a predefined threshold (s_{min}). Any pairs whose surfaces are closer than this limit will have the same energy as if the distance is s_{min} . The second model overcomes the divergence by considering the length of atomic bonds, effectively adjusting the separation distance in the energy expressions so that the divergence range is never reached. The third model involves replacing U_{vdw} , for small separations, with the cohesion energy combined with the Born-Mayer repulsion.

2.1. Model 1

In the first model, the van der Waals energy value decreases as the surface-surface distance moves towards its minimum cutoff value of $s_{min} = 0.01$ nm, and then it is held constant for smaller

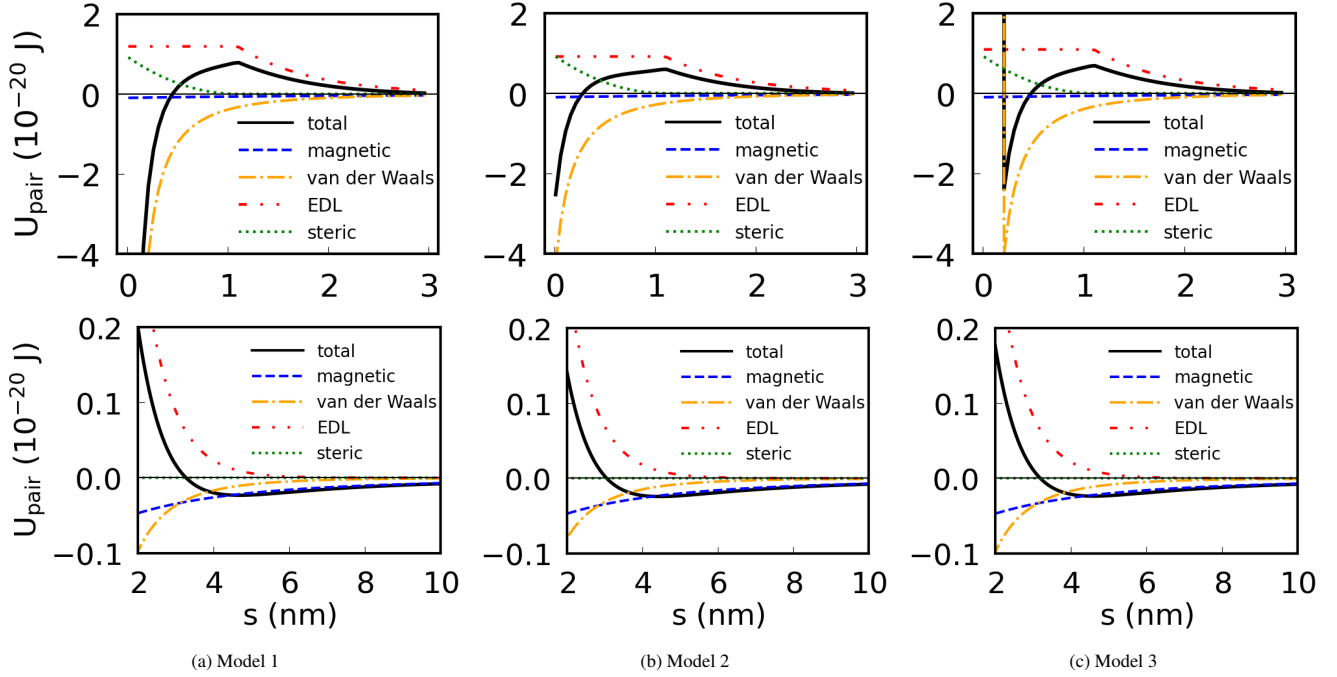


Figure 2: Total energy of a nanoparticle pair (U_{pair}), according to each model, as a function of the distance between their surfaces ($s \equiv s_{ij} = r_{ij} - 2R_{ij}$). The two particles are identical, with radii $R_i = R_j = 3.585$ nm ($= D_0/2$) and other parameters as given in Appendix A. The graphs in the top row show small distances (and consequently high energy values). In contrast, the graphs in the bottom row show the corresponding curves at larger distances (and low energy), evidencing the long-range nature of magnetic interactions. Models 2 and 3 have different strategies to deal with the divergence of the van der Waals energy, while it is barely treated in Model 1.

distances ($s < s_{min}$). The van der Waals energy between two particles R_i and R_j is written as [32]

$$U_{vdw}(r_{ij}) = -\frac{A}{6} \left[\frac{2R_i R_j}{r_{ij}^2 - (R_i + R_j)^2} + \frac{2R_i R_j}{r_{ij}^2 - (R_i - R_j)^2} + \ln \left(\frac{r_{ij}^2 - (R_i + R_j)^2}{r_{ij}^2 - (R_i - R_j)^2} \right) \right]. \quad (7)$$

The value of s_{min} was set as 0.01 nm, such that the van der Waals energy exhibits a deep well, as shown in Figure 2a.

The electrostatic repulsion is described using the linear superposition model [33], adapted to the fact that the surface charge is at the surfactant layer extremity:

$$U_{edl}(r_{ij}) = 4\pi k_B T (2\rho_{ion}) \lambda_D \frac{[4R_i^* \tanh(\frac{e\psi_i}{4k_B T})][4R_j^* \tanh(\frac{e\psi_j}{4k_B T})]}{r_{ij}} \times \exp\left(-\frac{r_{ij} - R_i^* - R_j^*}{\lambda_D}\right), \quad (8)$$

where

$$\begin{aligned} R_i^* &= R_i + \delta, \\ R_j^* &= R_j + \delta, \end{aligned} \quad (9)$$

are the effective nanoparticles radii adjusted by δ , the thickness of the surfactant layer (the length of the molecules), k_B is the Boltzmann constant, T is the absolute temperature, e is the elementary charge, ψ_i and ψ_j are the values of electric potential on the surfaces of the nanoparticles, s_σ is the distance between the charged

surfaces, and λ_D is the Debye length, given by

$$\lambda_D = \left(\frac{\epsilon k_B T}{(2\rho_{ion}) z_{ion}^2 e^2} \right)^{1/2}, \quad (10)$$

where ϵ is the electrical permittivity of the solvent, ρ_{ion} is the ion concentration of the solvent, and z_{ion} is the valence of the ions in the solution (we have used $z_{ion} = 1$ in this work).

The values of ψ_i (and ψ_j) were calculated as [34]

$$\psi_i = \frac{k_B T}{ze} \operatorname{acosh} \left(\frac{\sigma_i^2}{4\epsilon \rho_{ion} k_B T} \right), \quad (11)$$

where σ_i is the nanoparticle surface charge density, calculated through the relation [30]

$$\sigma_i = \left[ze \left(\frac{R_i}{R_i + \delta} \right)^2 \right] \xi, \quad (12)$$

which expresses the linear relation between the surface charge density and the surfactant density (ξ), considering that each surfactant molecule contributes with a charge ze at its extremity, located at a distance δ from the nanoparticle surface.

Figure 2a shows the contributions to the interaction energy between two nanoparticles with varying intersurface distance, as appearing in Model 1.

2.2. Model 2

The second model considers the length of a typical atomic bond in the nanoparticle bulk (L_B) and prevents the divergence of the van der Waals energy by adding to the intersurface distance

of the colloidal particle pairs, which is equivalent to changing the center-to-center distance as in

$$r_{ij} \rightarrow r_{ij} + L_B. \quad (13)$$

This procedure is similar to a modification tested by White [35] for the van der Waals interaction between planes.

Thus, the van der Waals energy between the nanoparticles i and j is then written as

$$U_{vdw}(r_{ij}) = -\frac{A}{6} \left[\frac{2R_i R_j}{(r_{ij} + L_B)^2 - (R_i + R_j)^2} + \frac{2R_i R_j}{(r_{ij} + L_B)^2 - (R_i - R_j)^2} + \ln \left(\frac{(r_{ij} + L_B)^2 - (R_i + R_j)^2}{(r_{ij} + L_B)^2 - (R_i - R_j)^2} \right) \right]. \quad (14)$$

For the sake of consistency, the same modification is applied to the EDL interaction:

$$U_{edl}(r_{ij}) = 4\pi k_B T (2\rho_{ion}) \lambda_D \frac{\left[4R_i^* \tanh\left(\frac{e\psi_i}{4k_B T}\right) \right] \left[4R_j^* \tanh\left(\frac{e\psi_j}{4k_B T}\right) \right]}{r_{ij} + L_B} \times \exp\left(-\frac{r_{ij} + L_B - R_i^* - R_j^*}{\lambda_D}\right). \quad (15)$$

The values of ψ_i (and ψ_j) are given by Eq. 11, as in Model 1.

Figure 2b presents the interaction energy between two nanoparticles according to Model 2.

2.3. Model 3

Another approach consists of replacing, for small separations, the van der Waals energy with the Born-Mayer repulsion and the cohesion energy [36], so that the expression for the joint expression looks like

$$U_{vdw-bm}(r_{ij}) = \begin{cases} U_{vdw}(r_{ij}) & \text{if } r_{ij} > R_{ij} + L_B, \\ U_{vdw}(L_B) + U_{coh}(r_{ij}) + U_{bm}(r_{ij}) & \text{otherwise,} \end{cases} \quad (16)$$

where $U_{vdw}(L_B)$ is the value of $U_{vdw}(r_{ij})$ for $r_{ij} = L_B$ (value shown in Appendix A), U_{bm} is the energy related to the Born-Mayer repulsion [37], given by

$$U_{bm} = A_{bm} \exp\left(-\frac{r_{ij} - R_{ij}}{L_{bm}}\right), \quad (17)$$

and

$$U_{coh} = A_{int} W_{coh}, \quad (18)$$

where A_{int} is the area between the spheres in which their surfaces are close enough to form atomic bonds (details of the calculation were shown in a previous article [36]) and W_{coh} is the cohesion work (value shown in Appendix A).

The authors also propose a change in the electrostatic interaction energy that makes it accurate at all distances, using a technique introduced by Schnitzer and Morozov [38]. The resulting expression is

$$U_{edl-sm}(r_{ij}) = -4\pi k_B T (2\rho_{ion}) \lambda_D \left[4R_i^* \tanh\left(\frac{e\psi_i}{4k_B T}\right) \right] \left[4R_j^* \tanh\left(\frac{e\psi_j}{4k_B T}\right) \right] \times e^{(R_i+R_j)/\lambda_D} Ei\left(-\frac{r_{ij} - 2\delta}{\lambda_D}\right), \quad (19)$$

where ρ_{ion} is the concentration of ions in the solvent, ψ_i and ψ_j are the electrical potential values on the surfaces of the spheres, Ei is the exponential integral function, and λ_D is the Debye length.

The energy curves of Model 3 are depicted in Figure 2c. Although the energy curves provided by the three models are very similar for long distances (bottom row of Figure 2), they exhibit significant differences for short distances (top row) in terms of shape and minimum value. Therefore, the models represent the colloid using distinct physical descriptions that we shall compare in the results of this study.

3. Simulation

The system was studied using Monte Carlo simulations, through an adaptation of the Metropolis-Hastings algorithm. Each simulation starts with a random configuration and small changes in the particle positions and orientations are made in successive steps. A newly generated configuration is accepted whenever the system energy decreases. If the energy increases by ΔE , the new configuration is accepted with a probability proportional to $\exp(-\beta\Delta E)$, with $\beta = (k_B T)^{-1}$. The scale of such changes is dynamically adjusted such that 50% of the generated configurations are accepted, by following the algorithm rules. After every 50 000 steps, the program calculates how much the ever-reached minimum value of total energy has decreased: sampling begins when this variation is less than 0.05, continues for at least other 50 000 steps, and finishes when the variation is less than 0.005. Those parameters are summarized in Appendix A. The quantities of interest are averaged over the sampling steps of at least ten independent simulations with each set of physical parameters.

Initially, we assess the total energy extensivity of the three models, as a form of validating them. This was done by simulating the colloidal solutions with increasingly higher particle number and evaluating its corresponding energy. The particle concentration was kept constant at 5% (volume fraction ϕ), a relatively high value that forces more particles into small separations. The interactions between the nanoparticles are higher in this regime, allowing a better evaluation of the system deviation from extensivity. After that, we simulated the ferrofluid at a lower concentration of $\phi = 0.47\%$, which was investigated in detail in our experimental reference [30]. The simulations included some variations as a means of comparing the effects of the characteristics and conditions of the colloid: monodisperse and polydisperse diameter distributions; non-magnetic and magnetic particles; and zero and finite applied magnetic fields. Other parameters are shown in Appendix A.

4. Results and discussion

Figure 3 presents the ferrofluid total energies for growing particle size, considering the three different models for both mono- and polydisperse solutions. The error bars results from the variability of different Monte Carlo executions. The curves are fitted according to a quadratic equation $f(N) = a + bN + cN^2$, with no intercept coefficient ($a = 0$). Note that the best fits yield small values for the quadratic coefficients, indicating an approximately linear energy scaling. Note that all except the model 3 monodisperse show a negative slope.

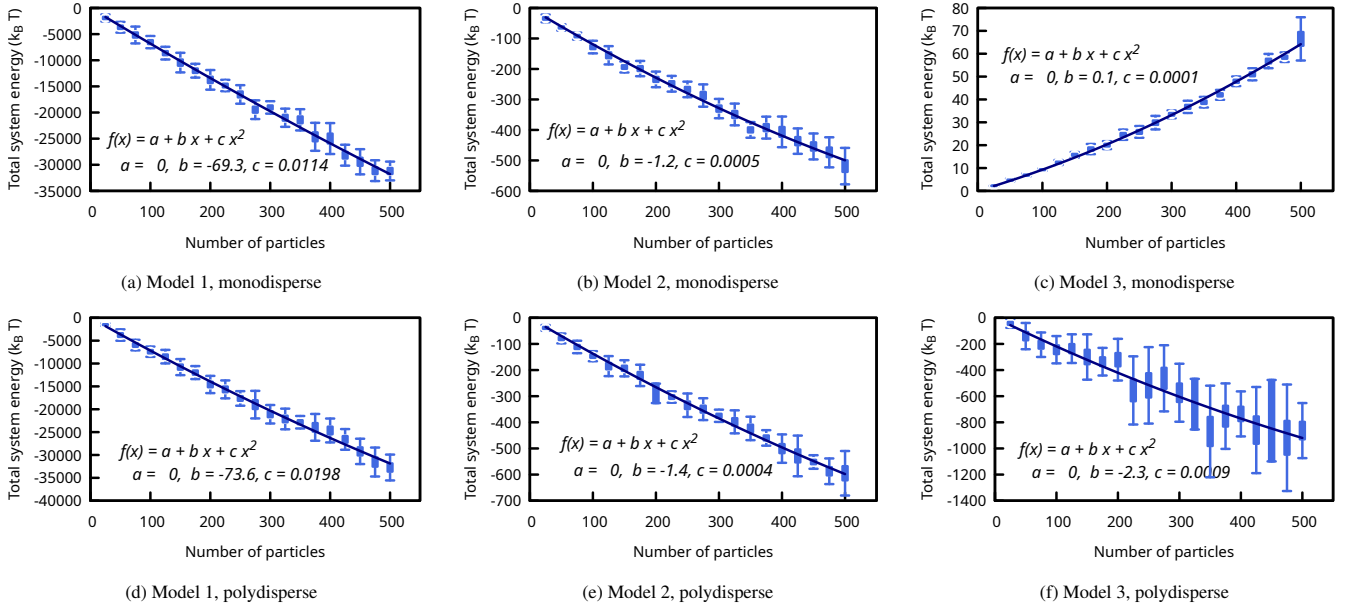


Figure 3: Total energy of the magnetic colloid versus the number of particles, for the three models, at a volume fraction of 5%. The modal radius is $R_0 = 3.585$ nm, with a log-normal distribution with dispersion $\sigma_R = 0.12$ for the polydisperse systems. The candlesticks represent the standard error and standard deviation around each value. The small values of the parameter c suggest that the dependence is approximately linear, which means that the total energy may be regarded as an extensive quantity despite the long-range interactions.

Table 1: Comparison of the energy terms from the best fits ($f(N) = a + bN + cN^2$, with $a = 0$) of the curves from 3, for $N = 500$. The last column shows the proportion of the total energy represented by the quadratic term. The higher deviations from linearity are observed in the monodisperse samples when simulated through Model 2 and Model 3.

Model	Energy terms (J)		
	$ bN $	$ cN^2 $	$\frac{ cN^2 }{ bN+cN^2 }$
Monodisperse samples			
1	34 650	2850	0.09
2	600	125	0.26
3	50	25	0.33
Polydisperse samples			
1	36 800	4950	0.16
2	700	100	0.17
3	1150	225	0.24

Model 3 contrasts with the other models for giving a positive total energy value for the monodisperse system, indicating an overall repulsion between the nanoparticles, a clear consequence of the Born-Mayer interaction. However, for the polydisperse system, the total energy is negative as in the other cases, a consequence of the higher magnetic dipolar and van der Waals attractions between the large particles that are present in the polydisperse colloids. One can also note more energy fluctuations for the polydisperse system simulated with Model 3, when compared to the other models, indicating freedom to reach more diverse configurations.

Interestingly, direct comparison of the linear (bN) and quadratic (cN^2) terms, as shown in Table 1, reveals that the quadratic term of the model 3 monodisperse case reaches a third of the value of the total energy. This particle sample is near the threshold being globally repulsive (with overall posi-

tive interaction energy) and globally attractive (negative energy) regimes, causing small values of the linear term, as shown in Figure 3c. Some non-extensive behavior might be observable in such a monodisperse system, although not in the real polydisperse system that was studied experimentally [30].

Jund et al. [39] analyzed the extensivity of a simplified ferrofluid model, with magnetic dipolar interaction and a non-magnetic term given by

$$u^{nm}(r_{ij}) = \epsilon \left[\left(\frac{\sigma}{r_{ij}} \right)^\rho - \left(\frac{\sigma}{r_{ij}} \right)^\alpha \right], \quad (20)$$

with $0 \leq \alpha \leq \rho \leq \infty$. The authors concluded that “extensive thermodynamics” is applicable for the case $\alpha > 1$, with the energy being approximately directly proportional to the number of particles. In our models, the van der Waals interaction serves as the second term of the equation 20, that is, the attractive part of the interaction. An analysis of Equation 8 shows that the van der Waals attraction corresponds approximately to the case $\alpha = 2$, which explains the near linearity observed between energy and number of particles for most samples, despite the relatively high particle concentration.

Additional insights can emerge when explicitly analyzing the interaction energy profiles of each model. Supplementary Figure S1 displays the total energies (and the individual contributions) for solutions with different nanoparticle sizes in the short-range regime. As we can see in Figure 2, the curves for Models 1 and 2 diverge significantly at atomic-level distances, while Model 3 remains limited. Moreover, the magnetic interactions are considerably weaker than all the other terms. The steric interaction exhibits similar behavior at distances above 1 nm. Looking at energy profiles for larger distances, we see that the secondary energy minimum around 4 nm becomes more pronounced as we increase particle radius because doing so increases the strength

of magnetic attraction (Supplementary Figure S2).

To characterize the colloidal structural organization, it is crucial to investigate the properties of the secondary minima using the different models. Varying the radii of two interacting particles, we observe, for the three models, that the surface-surface separation associated with minimal energy decreases as the particles' radii increase (Figures S2 and S3). More generally, for any combination of different radii of particles in a pair, increasing any of the two radii leads to a decreased minimal energy particle separation. Increasing the radius of either particle in an interacting pair also leads to a deepening of the potential energy profile around the minimum energy point, as one can see in Supplementary Figure S3. Of course, these observations can be explained through the increase in magnetic attraction associated with increasing the particle size.

We compare these models more directly by looking at the relative difference between models 2 and 3 compared to model 1, which is an established formalism in colloid simulations. In panels (a) and (b) of Supplementary Figure S4, one can see that the relative difference between Models 1 and 2 presents a higher variability over the space of particles' radii combinations, while Model 3 differs from Model 1 through a more systematic and better-conserved shift, at least regarding the equilibrium particle distance. Still, Models 2 and 3 predict equilibrium distances smaller than those predicted by Model 1.

The highest variations for Model 2, for sets where the sum $R_i + R_j$ is constant, occur when $R_i = R_j$. In other words, the distinction between Model 2 and Model 1 is more pronounced in the monodisperse case (look at the diagonal of Figure S4(a)) than in the polydisperse case. Similar conclusions apply to the energy, as shown in Figures S4(c) and S4(d) for Model 2 and Model 3, respectively. A point worth mentioning is that in all cases the energy depth increased, indicating an improved description of agglomeration mechanisms. The stronger secondary minimum may serve as a competing factor in the formation of strongly bound nanoparticles that were artificially trapped in the first minimum in Model 1.

Another quantity of interest is the average first-neighbor distance ($\langle s_1 \rangle$), calculated as the mean (over all particles) of the distance between each particle and its nearest neighbor particle. This quantity does not depend on definitions of "bonded particles", typically based on distance or energy thresholds. By choosing $\langle s_1 \rangle$ in our analysis, we avoid using such thresholds, whose definition inevitably requires some arbitrariness. Table 2 shows $\langle s_1 \rangle$ for the monodisperse and polydisperse samples, simulated through the three models, at the particle concentration (volume fraction) of $\phi = 5\%$. The dependence of $\langle s_1 \rangle$ with the number of particles considered in the simulations is shown in the Support Information). Model 1 and Model 2 show that the nanoparticles are generally more distant from their first neighbors in the polydisperse system. This may be explained by the fact that the EDL repulsion increases faster than the magnetic dipolar and van der Waals attraction with increasing diameters in the short range. The log-normal distribution is skewed towards larger diameters, which favors both higher barriers that prevent nanoparticles from reaching the primary energy minima (see the short-range graphs in the Support Information). Model 3 resulted in more sparse nanoparticles, as an effect of the short-range repulsions. However, in contrast with the other models, the values of $\langle s_1 \rangle$ are now

Table 2: Average first neighbor distance ($\langle s_1 \rangle$) for monodisperse and polydisperse systems, at a volume fraction of 5% simulated through different models, with standard errors. The short-range repulsions of Model 3 caused overall higher values, especially for the monodisperse system (in contrast with the other models, with higher distances for the polydisperse system).

Model	Average first neighbor distance (nm)	
	monodisperse	polydisperse
1	2.17 ± 0.04	2.61 ± 0.04
2	2.06 ± 0.05	2.57 ± 0.05
3	3.12 ± 0.06	2.74 ± 0.04

Table 3: Average first neighbor distance ($\langle s_1 \rangle$) for the monodisperse systems simulated through different models, with standard errors, at a volume fraction of 0.47% [30]. The values given by Model 3 are slightly higher, with a more significant disagreement with the other models, considering the standard errors.

Model	Average first neighbor distance (nm)		
	non-magn.	magnetic $B = 0$ T	magnetic $B = 1$ T
1	11.88 ± 0.07	12.24 ± 0.98	12.11 ± 0.09
2	11.80 ± 0.08	11.94 ± 0.17	12.24 ± 0.92
3	12.45 ± 0.55	12.37 ± 0.75	12.34 ± 0.87

higher for the monodisperse system. This result agrees with the energy curves shown in Figure 3 and can be better explained by the position of the secondary energy minima, which occurs in shorter distances for larger particles.

We also analyzed this quantity for the ferrofluid at the lower volume fraction of 0.47% which characterizes the real sample [30]. Table 3 and Table 4 show the values of $\langle s_1 \rangle$ for non-magnetic colloids, magnetic colloids with zero applied magnetic field, and magnetic colloids subject to an applied field of one tesla. In this regime, the average first-neighbor distance is higher, such that the small-range repulsions included in Model 3 are only relevant for a minority of the nanoparticles. Thus, all models yield higher values of $\langle s_1 \rangle$ for the polydisperse systems, when compared to the monodisperse ones. This is caused by the higher EDL repulsion provided by larger particles, which reduces the occurrence of pairs trapped in the primary minima. The differences between the $\langle s_1 \rangle$ values for non-magnetic colloid, magnetic colloid at zero field, and magnetic colloid at 1 T are barely noticeable. Our focus is on the nanoparticle interactions, more easily studied in the magnetic colloid at zero field.

The results also include the pair correlation function $g(r)$, shown in Figure 4 for mono (a) and polydisperse (b) systems in the zero field condition for the three models. As expected,

Table 4: Average first neighbor distance ($\langle s_1 \rangle$) for the polydisperse system simulated through different models, with standard errors. The differences between the values are negligible, except for the slightly higher values of Model 3 for the non-magnetic system. This is explained by the larger particles that increase the EDL repulsion, which, in magnetic colloids, is counterbalanced by the increase of the magnetic dipolar attraction.

Model	Average first neighbor distance (nm)		
	non-magn.	magnetic $B = 0$ T	magnetic $B = 1$ T
1	13.31 ± 0.12	13.47 ± 0.12	13.42 ± 0.11
2	13.50 ± 0.13	13.20 ± 0.13	13.44 ± 0.11
3	13.61 ± 0.09	13.76 ± 0.13	13.75 ± 0.09

the peak heights are proportional to the energy well depths, with Model 1 resulting in higher peaks and Model 3 in lower ones. The polydisperse systems present more dispersed peaks, as a result of the statistical variability of the nanoparticle diameters, making multiple separation distances available depending on the radii of the pairs.

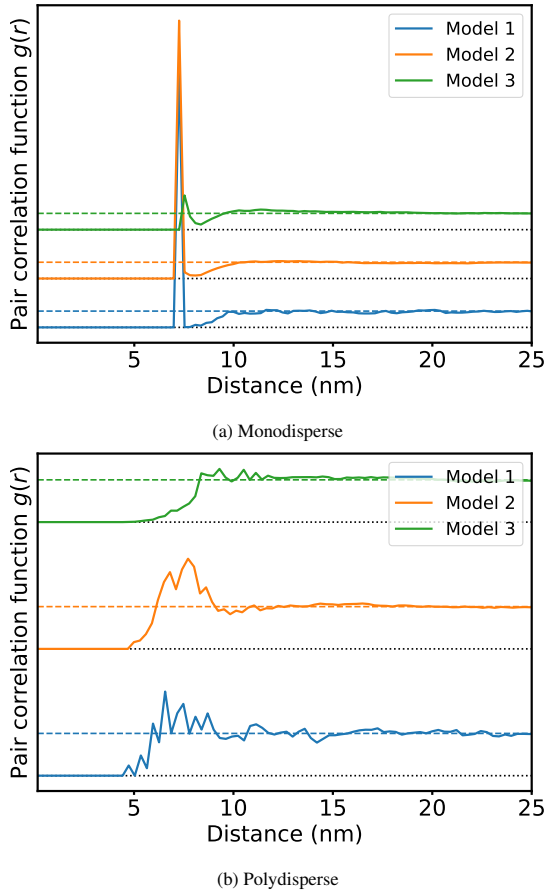


Figure 4: Pair correlation function for the mono and polydisperse systems in the zero field condition, simulated through the three models. Higher peaks are observed for Models 1 and 2, and the lowest ones with Model 3. Diameter polydispersity makes the peaks more dispersed.

The interaction between magnetic particles depends on their positions and orientations, as defined by their magnetic moment dipoles. Thus, we also computed the angular pair correlation function $g(r, \theta)$, shown as heatmaps in Figure 5. The horizontal axis ($\theta = 0^\circ$) in the heatmaps coincides with the z -axis of a coordinate system xyz . Brighter regions indicate a higher probability of encountering a pair of particles separated by a distance r at an angle θ relative to the z -axis. The darker regions at the centers appear because r is the distance between the centers of two particles, and the nanoparticles are hard spheres whose volumes do not overlap. The yellow ring between $r = 5$ and $r = 10$ for the monodisperse systems is associated with the first neighbor distance, bounded from below by the particle diameter. For polydisperse systems, the minimum distance between two particles' centers can vary significantly and, therefore, we no longer have such a characteristic first-neighbor-distance ring.

There is a prominent contrast in $g(r, \theta)$ when comparing the different models. For both poly and monodisperse solutions, the

heatmaps from Models 2 and 3 are significantly smoother than those from Model 1. The bright spots in Model 1 (Figures 5a and 5d) are the result of diverging attractive short-range interactions that trap pairs of nanoparticles in their interaction potential wells.

The highly negative energy values that arise in this situation cause a generally reduced mobility of the particles in the Monte Carlo simulation. That happens because when there are interactions with different orders of magnitude, the algorithm prioritizes changes in nanoparticles that most affect the dominant interaction. As a result, the total energy reaches a deep local minimum. The remaining components lose part of their influence in determining the colloidal stationary configuration due to the difference in magnitude. Consequently, finding the global minimum becomes numerically challenging, as changes in the non-dominant interactions produce negligible effects on the total energy. In other words, when the interaction energy between a particle pair is too negative, other particles may also “freeze” in energetically unfavorable configurations.

The heatmaps for Models 2 and 3 in turn do not have such prominent spots, presenting only barely discernible lighter regions near the central ring. For Model 2, this result is attributed to the higher EDL repulsion involving larger colloidal particles, which prevents configuration freezing, thus allowing particles to move towards the main minimum of pair interactions.

For Model 3, adopting the Born-Mayer repulsion and the cohesion energy for small separations avoids the implicit assumptions of the van der Waals energy expressions, which commonly do not apply near the microscopic scale. Besides this physical motivation that can provide some trust in these corrections used in Model 3, we observe this model also presents better Monte Carlo sampling properties. This, in turn, leads to a higher level of confidence in results obtained from Model 3, due to better-assured convergence of simulations.

Our results show that an inadequate application of energy models may not only give wrong values for the system energy and other physical quantities but also lead to an unexpected behavior of the simulation algorithm. This has practical implications for modeling agglomeration effects in colloids. Relying on a simplified pair energy function may result in a poor description of the mechanism. In contrast, using a more refined approach could not only offer a better representation but also more accurately identify the conditions that lead to these states.

5. Conclusion

We simulated a ferrofluid with biomedical interest, composed of magnetite nanoparticles surface-coated with tartrate acid and dispersed in water, and compared different strategies for dealing with the limitations of the DLVO theory at the small distances between colloidal particle surfaces. The colloid was simulated through Monte Carlo simulations using three models of nanoparticle pair interaction. For the sake of comparison, the simulations include variations of the system: magnetic and non-magnetic colloid, with diameter monodispersity and polydispersity at zero and finite field conditions.

As long-range interactions might result in a system with non-extensive energy, we investigated the total energy variation with the number of particles, for a high-density ferrofluid solution. The results showed an approximate linearity for almost all the

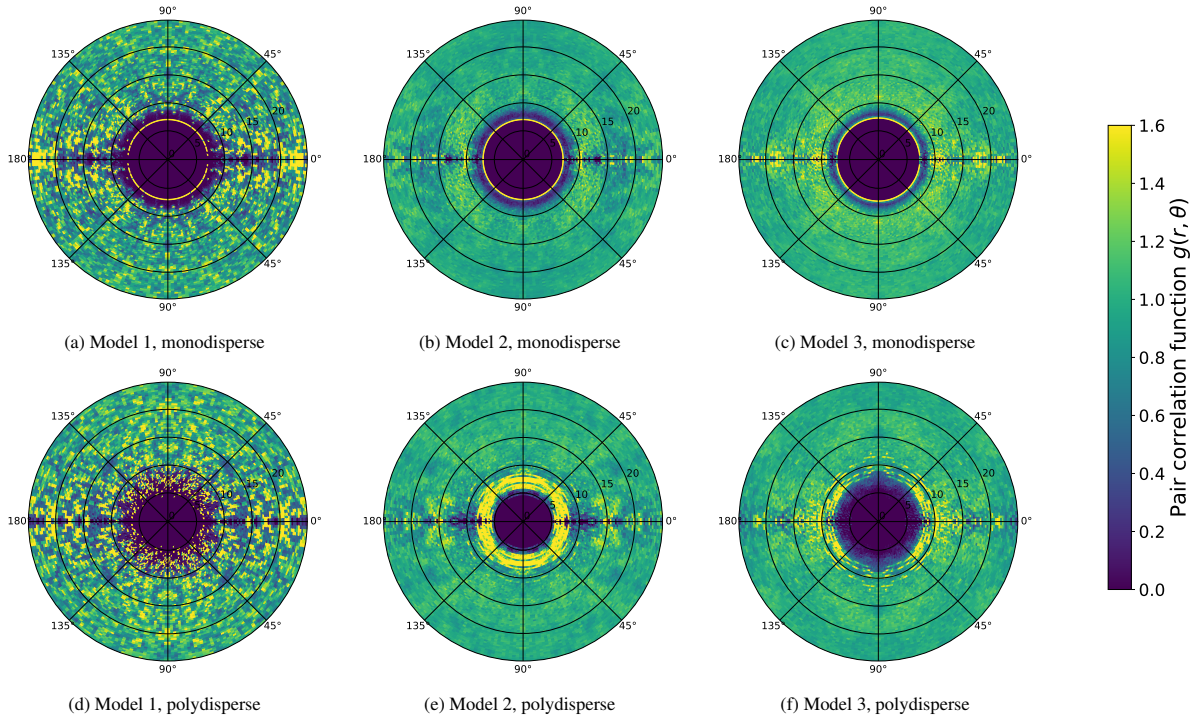


Figure 5: Pair correlation function $g(r, \theta)$, simulated through the three models, for magnetic systems at zero applied field condition, with diameter monodispersity and polydispersity, at volume fraction $\phi = 0.47\%$. r is in units of nanometers. The spots observed for Model 1 are caused by particle pairs trapped in local minima or the deep well as their surfaces approach each other. Light areas along the horizontal axis are better distinguished for Model 2 and Model 3. This highlights the relevant influence of polydispersity on the magnetic structure. For improved visualization, the colormap is limited to 1.6, and all points with $g(r, \theta) > 1.6$ are shown in the same color. For instance, the height of the central yellow rings for monodisperse systems should correspond to the peaks observed in Figure 4a.

models studied. The only exception is the third model in monodisperse configuration, which contains a revised van der Waals interaction for small distances using the Born-Mayer repulsion and cohesion energies. This case is a borderline between the globally repulsive and globally attractive regimes, causing smaller absolute energy values. The real samples experimentally investigated have diameter polydispersity, which could present non-extensive thermodynamic behavior found in the results.

The colloidal structure was assessed through the average first-neighbor distance, the pair correlation function, and the angular pair correlation function. The results showed that a more detailed microscopic model, which replaces the van der Waals attraction with the cohesion energy and the Born-Mayer repulsion at small surface-surface distances, describes the balance between magnetic and other nanoparticle interactions more realistically. This approach is even more important for samples with polydisperse diameters, which include larger nanoparticles.

In simulations with deep wells in the van der Waals curve, many particle pairs fall into local minima, reducing the overall mobility of other particles during the simulations, thus causing bias in the sampling process. This might render the simulation results questionable for comparison with data from experiments. The microscopically detailed energy model presented here aids in our understanding of the balance between repulsive and attractive interactions amongst colloidal particles. This knowledge will be helpful in the design of biocompatible colloids and, in particular, biocompatible ferrofluids, considering their intended applications.

Supporting Information

Supplementary files associated with this article can be found in the online version.

Appendix A. Parameters

Table A.5: Metropolis-Hasting algorithm.

Variable	Description	Value
$N_{MC\{max\}}$	maximum number of MC steps	300 000
$N_{MC\{chk\}}$	number of MC steps between convergence checks	50 000
ΔU_{ini}	energy variation to begin sampling	0.05
ΔU_{fin}	energy variation to finish sampling	0.005
α	target acceptance rate in Metropolis algorithm	0.5
s_{min}	surface minimum distance	0.01 nm
N	number of particles in the box	25 (minimum) 500 (maximum) [30]

Table A.6: Dispersed phase: magnetite nanoparticles.

Parameters	Description	Value
D_0	modal diameter	7.17 nm
R_0	modal radius	3.585 nm [30]
σ_D	diameter dispersion	0.24
σ_R	radius dispersion	0.24 [30]
M	magnetization	$4.71 \times 10^5 \text{ A m}^{-1}$ [30]
ξ	grafting parameter	$2.0 \times 10^{17} \text{ m}^{-2}$ [30]
δ	surfactant layer length	0.55 nm [30]
δ_s	excluded radius	0.8 nm
W_{coh}	cohesion energy (maghemite)	1.38 J m^{-2} [40]
L_B	atomic bond distance (maghemite Fe–O)	0.19 nm [41, 42]
A_{bm}	Born-Mayer parameter A	1207.6 eV [37]
L_{bm}	Born-Mayer parameter L	0.3084 Å [37]
λ_D	Debye length	1.1 nm [30]

Table A.7: Dispersion medium: water.

Parameters	Description	Value
μ	magnetic permeability	$1.26 \times 10^{-6} \text{ H m}^{-1}$
ρ_{ion}	ion concentration	0.15 mol L ⁻¹ [30]

Table A.8: Colloid: magnetite particles in water.

Parameters	Description	Value
ϕ	volume fraction	0.05 (5%) 0.0047 (0.47%) [30]
T	temperature	300 K [30]
A	Hamaker constant	$0.40 \times 10^{-21} \text{ J}$ [30]

References

- [1] R. L. Bailey, “Lesser known applications of ferrofluids,” *Journal of Magnetism and Magnetic Materials*, vol. 39, p. 178, 1983.
- [2] K. Raj and R. Moskowitz, “Commercial applications of ferrofluids,” *Journal of Magnetism and Magnetic Materials*, vol. 85, no. 1, pp. 233–245, 1990.
- [3] J. Roger, J. N. Pons, R. Massart, A. Halbreich, and J. C. Bacri, “Some biomedical applications of ferrofluids,” *The European Physical Journal - Applied Physics*, vol. 5, no. 3, pp. 321–325, 1999.
- [4] C. Scherer and A. M. Figueiredo, Neto, “Ferrofluids: properties and applications,” *Brazilian Journal of Physics*, vol. 35, no. 3A, p. 718, 2005.
- [5] G. Song, M. Kenney, Y. S. Chen, X. Zheng, Y. Deng, Z. Chen, S. X. Wang, S. S. Gambhir, H. Dai, and J. Rao, “Feco/graphitic-shell nanocrystals as advanced magnetic-resonance-imaging and near-infrared agents,” *Nat. Mater.*, vol. 5, pp. 971–976, 2006.
- [6] M. G. Harisinghani, J. Barentsz, P. F. Hahn, W. M. Deserno, S. Tabatabaei, C. H. van de Kaa, J. de la Rosette, and R. Weissleder, “Noninvasive detection of clinically occult lymph-node metastases in prostate cancer,” *N. Engl. J. Med.*, vol. 348, pp. 2491–2499, June 2003.
- [7] G. Song, M. Kenney, Y. Chen, X. Zheng, Y. Deng, Z. Chen, S. Wang, S. Gambhir, H. Dai, and J. Rao, “Carbon-coated feco nanoparticles as sensitive magnetic-particle-imaging tracers with photothermal and magnetothermal properties,” *Nat Biomed Eng*, vol. 4, no. 3, 2020.
- [8] C. Alexiou, R. Schmid, R. Jurgons, C. Bergemann, W. Arnold, and F. G. Parak, “Targeted tumor therapy with magnetic drug targeting,” in *Ferrofluids: magnetically controllable fluids and their applications*, pp. 233–251, Ed. Stefan Odenbach, 2002.
- [9] U. Maver, M. Bele, D. Makovec, S. Čampelj, J. Jamnik, and M. Gaberšček, “Incorporation and release of drug into/from superparamagnetic iron oxide nanoparticles,” *Journal of Magnetism and Magnetic Materials*, vol. 321, no. 19, pp. 3187–3192, 2009.
- [10] M. Sato, T. Yamashita, M. Ohkura, Y. Osai, A. Sato, T. Takada, H. Matsusaka, I. Ono, Y. Tamura, N. Sato, Y. Sasaki, A. Ito, H. Honda, K. Wakamatsu, S. Ito, and K. Jimbow, “N-propionyl-cysteaminyphenol-magnetite conjugate (nprcap/m) is a nanoparticle for the targeted growth suppression of melanoma cells,” *Journal of Investigative Dermatology*, vol. 129, no. 9, pp. 2233–2241, 2009.
- [11] E. L. Verde, G. T. Landi, J. A. Gomes, M. H. Sousa, and A. F. Bakuzis, “Magnetic hyperthermia investigation of cobalt ferrite nanoparticles: Comparison between experiment, linear response theory, and dynamic hysteresis simulations,” *J. Appl. Phys.*, vol. 111, p. 123902, June 2012.
- [12] M. Santos Carrião and A. Bakuzis, “Mean-field and linear regime approach to magnetic hyperthermia of core-shell nanoparticles,” *Nanoscale*, vol. 8, pp. 8363–8377, 2016.
- [13] G. N. Rego, J. B. Mamani, T. K. Souza, M. P. Nucci, H. R. Silva, and L. F. Gamarra, “Therapeutic evaluation of magnetic hyperthermia using fe₃o₄-aminosilane-coated iron oxide nanoparticles in glioblastoma animal model,” *Einstein (São Paulo)*, vol. 17, no. 4, p. eAO4786, 2019.
- [14] M. S. Gopika, B. B. Lahiri, B. Anju, J. Philip, and S. S. Pillai, “Magnetic hyperthermia studies in magnetite ferrofluids based on bio-friendly oils extracted from calophyllum inophyllum, brassica juncea, ricinus communis and madhuca longifolia,” *Journal of Magnetism and Magnetic Materials*, vol. 537, p. 168134, 2021.

- [15] E.-A. Moacă, V. Socoliuc, D. Stoian, C. Watz, D. Flondor, C. Păcurariu, R. Ianoș, C. I. Rus, L. Barbu-Tudoran, A. Semencescu, *et al.*, “Synthesis and characterization of bioactive magnetic nanoparticles from the perspective of hyperthermia applications,” *Magnetochemistry*, vol. 8, no. 11, p. 145, 2022.
- [16] Y. Patil-Sen, “Advances in nano-biomaterials and their applications in biomedicine,” *Emerging Topics in Life Sciences*, vol. 5, no. 1, pp. 169–176, 2021.
- [17] K. Ono, Y. Matsukawa, Y. Saito, H. Aoki, K. Era, T. Aoki, and T. Yamaguchi, “Monte carlo simulation for morphology of nanoparticles and particle size distributions: comparison of the cluster–cluster aggregation model with the sectional method,” *Journal of Nanoparticle Research*, vol. 242, p. 242, 2015.
- [18] L. L. Castro, R. Miotto, and A. F. Bakuzis, “Concentration effects on the grafting of magnetic nanoparticles by Monte Carlo simulations,” *Journal of Applied Physics*, vol. 99, no. 08S101, 2006.
- [19] F. L. O. Paula, L. L. Castro, T. S. A. Cassiano, S. G. dos Santos, G. Gomide, J. Depeyrot, and A. F. C. Campos, “pH-dependent phase transitions in ferrofluids: A monte carlo simulation study using an extended dlvo model,” *Colloids and Surfaces A: Physicochemical and Engineering Aspects*, vol. 658, p. 130578, 2023.
- [20] G. Brancolini, V. M. Rotello, and S. Corni, “Role of ionic strength in the formation of stable supramolecular nanoparticle–protein conjugates for biosensing,” *International Journal of Molecular Sciences*, vol. 23, no. 4, 2022.
- [21] A. F. C. Campos, E. P. Marinho, A. Ferreira, F. A. Tourinho, F. L. O. Paula, and J. Depeyrot, “X-dlvo interactions between nanocolloidal magnetic particles: The quantitative interpretation of the ph-dependent phase diagram of edl-mf,” *Brazilian Journal of Physics*, vol. 39, pp. 230–235, 2009.
- [22] X. Deng, Z. Huang, W. Wang, and R. N. Davé, “Investigation of nanoparticle agglomerates properties using monte carlo simulations,” *Advanced Powder Technology*, vol. 27, no. 5, pp. 1971–1979, 2016.
- [23] D. Mostarac, Y. Xiong, O. Gang, and S. Kantorovich, “Nanopolymers for magnetic applications: how to choose the architecture?,” *Nanoscale*, vol. 14, no. 31, pp. 11139–11151, 2022.
- [24] G. Mériguet, M. Jardat, and P. Turq, “Structural properties of charge-stabilized ferrofluids under a magnetic field: A brownian dynamics study,” *The Journal of chemical physics*, vol. 121, no. 12, pp. 6078–6085, 2004.
- [25] F. L. de Oliveira Paula, “Saxs analysis of magnetic field influence on magnetic nanoparticle clusters,” *Condensed Matter*, vol. 4, no. 2, 2019.
- [26] M. A. Salvador, A. S. Costa, M. Gaeti, L. P. Mendes, E. M. Lima, A. F. Bakuzis, and R. Miotto, “Characterization, nanoparticle self-organization, and monte carlo simulation of magnetoliposomes,” *Phys. Rev. E*, vol. 93, p. 022609, Feb 2016.
- [27] J. Israelachvili, *Intermolecular e surface forces*. Academic Press, 1992.
- [28] F. L. O. Paula, R. Aquino, G. J. da Silva, J. Depeyrot, F. A. Tourinho, J. O. Fossum, and K. D. Knudsen, “Small-angle X-ray and small-angle neutron scattering investigations of colloidal dispersions of magnetic nanoparticles and clay nanoplatelets,” *Journal of Applied Crystallography*, vol. 40, pp. s269–s273, Apr 2007.
- [29] F. L. O. Paula, G. J. da Silva, R. Aquino, J. Depeyrot, J. O. Fossum, K. D. Knudsen, G. Helgesen, and F. A. Tourinho, “Gravitational and magnetic separation in self-assembled clay-ferrofluid nanocomposites,” *Brazilian Journal of Physics*, vol. 39, pp. 163 – 170, 04 2009.
- [30] A. F. Bakuzis, L. C. Branquinho, L. L. e Castro, M. T. de Amaral e Eloi, and R. Miotto, “Chain formation and aging process in biocompatible polydisperse ferrofluids: Experimental investigation and monte carlo simulations,” *Advances in Colloid and Interface Science*, vol. 191-192, pp. 1–21, 2013.
- [31] R. E. Rosensweig, *Ferrohydrodynamics*. Dover, 1997.
- [32] H. C. Hamaker, “The London – van der Waals attraction between spherical particles,” *Physica*, vol. 4, no. 10, p. 1058, 1937.
- [33] W. B. Russel, D. A. Saville, and W. R. Schowalter, *Colloidal Dispersions*. Cambridge Monographs on Mechanics, Cambridge University Press, 1989.
- [34] R. J. Hunter, “Colloid science,” in *Zeta Potential in Colloid Science* (R. H. Ottewill and R. L. Rowell, eds.), p. 386, Academic Press, 1981.
- [35] L. R. White, “van der waals interaction energy and disjoining pressure at small separation,” *Journal of Colloid and Interface Science*, pp. 338–343, 2010.
- [36] L. L. Castro, C. C. C. Amorin, P. V. Miranda, J. T. S. A. Cassiano, and F. L. O. Paula, “The role of small separation interactions in ferrofluid structure,” *Colloids and surfaces A*, vol. 635, no. 128082.
- [37] G. V. Lewis and C. R. A. Catlow, “Potential models for ionic oxides,” *Journal of Physics C: Solid State Physics*, vol. 18, pp. 1149–1161.
- [38] O. Schnitzer and M. Morozov, “A generalized derjaguin approximation for electrical-double-layer interactions at arbitrary separations,” *The Journal of Chemical Physics*, vol. 142, no. 24, p. 244102, 2015.
- [39] P. Jund, S. G. Kim, and C. Tsallis, “Crossover from extensive to nonextensive behavior driven by long-range interactions,” *Physical Review B*, vol. 52, no. 1.

- [40] I. I. Diakonov, “Thermodynamic properties of iron oxides and hydroxides. ii. estimation of the surface and bulk thermodynamic properties of ordered and disordered maghemite (γ -Fe₂O₃),” *European Journal of Mineralogy*, vol. 10, no. 1, pp. 17–30, 1998.
- [41] M. L. Fdez-Gubieda, A. García-Prieto, J. Alonso, and C. Meneghini, *X-Ray Absorption Fine Structure Spectroscopy in Fe Oxides and Oxyhydroxides*, ch. 17, pp. 397–422. John Wiley & Sons, Ltd, 2016.
- [42] M. Coduri, P. Masala, L. Del Bianco, F. Spizzo, D. Ceresoli, C. Castellano, S. Cappelli, C. Oliva, S. Checchia, M. Allietta, D.-V. Szabo, S. Schlabach, M. Hagelstein, C. Ferrero, and M. Scavini, “Local structure and magnetism of Fe₂O₃ maghemite nanocrystals: The role of crystal dimension,” *Nanomaterials*, vol. 10, no. 5, 2020.

Electronic Supplementary Information for: Effects of diameter polydispersity and small-range interactions on the structure of biocompatible colloidal nanoparticles[†]

Aimê Gomes da Mata Kanzaki¹, Tiago de Sousa Araújo Cassiano¹, João Pedro Valeriano Miranda^{*,2}, Fabio Luis de Oliveira Paula¹, and Leonardo Luiz e Castro¹

¹ *University of Brasília, Instituto de Física, Campus Universitário Darcy Ribeiro, Brasília, 70.910-900, DF, BR*

² *Aix-Marseille Université, CINAM, Turing Centre for Living Systems, Marseille, FR*

*joao-pedro.valeriano-miranda@univ-amu.fr

arXiv:2412.07719v1 [cond-mat.soft] 10 Dec 2024

Dependence of average first-neighbor distance with the number of particles in the simulation

Figure S1 shows $\langle s_1 \rangle$ versus the number of particles inside the simulation box for Model 1 (a), Model 2 (b) and Model 3 (c). The particle concentration (volume fraction) is $\phi = 5\%$.

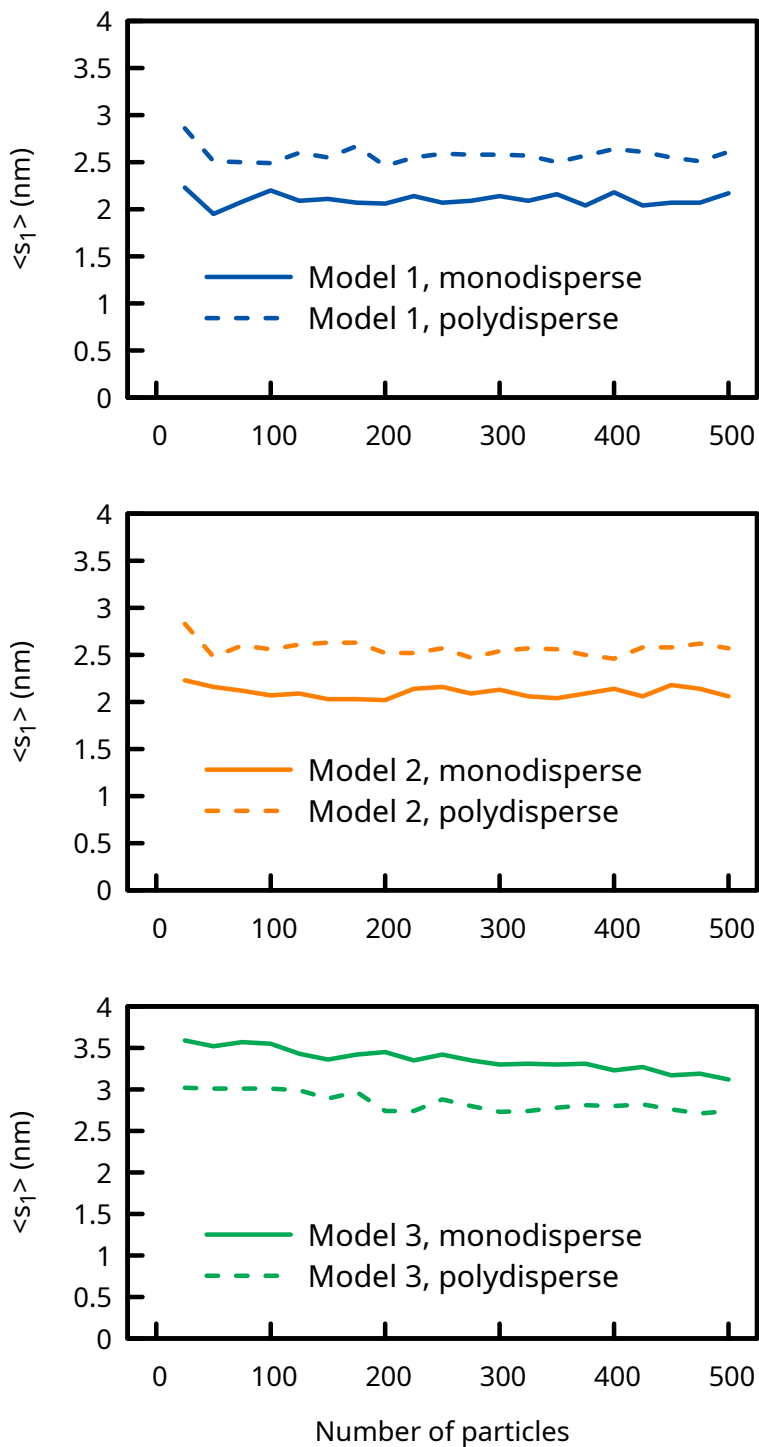


Figure S1: Average first-neighbor distance ($\langle s_1 \rangle$) versus number of simulated particles (N), for the system at a $\phi = 5\%$.

Interaction energy profiles from each model

The variation of the primary minimum radius depends on the particle radius only by a tiny margin, as one can conclude by comparing Figure S2. Thus, we made a deeper analysis of the secondary minimum, whose position and depth vary with the nanoparticle radii more significantly, as shown in Figure S3.

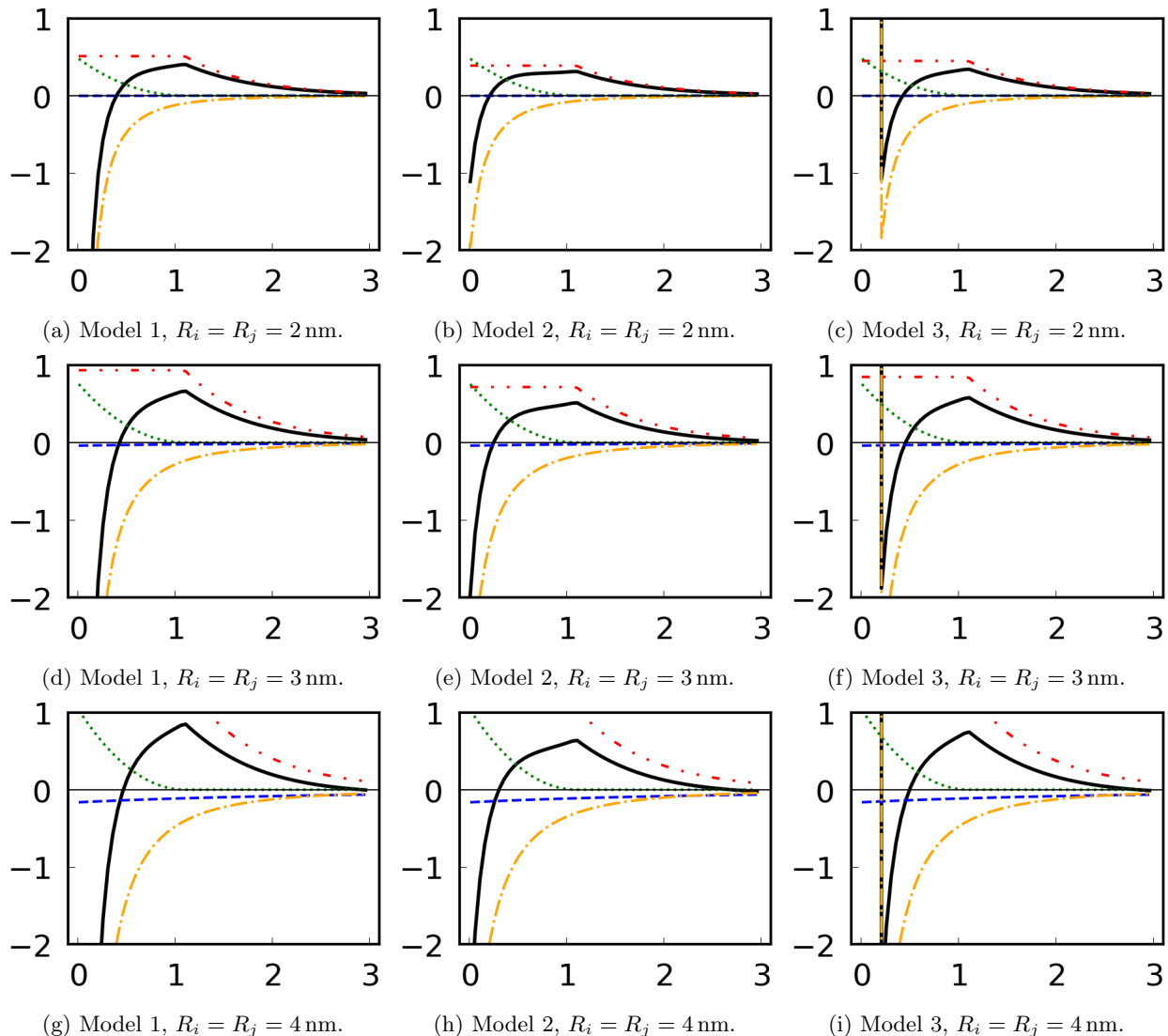


Figure S2: Interaction energy of two nanoparticles with equal radii in dependence on their intersurface distance, in the short range (0 nm to 3 nm), for the models 1, 2 and 3, from left to right. Other nanoparticle parameters are as shown in the article appendices.

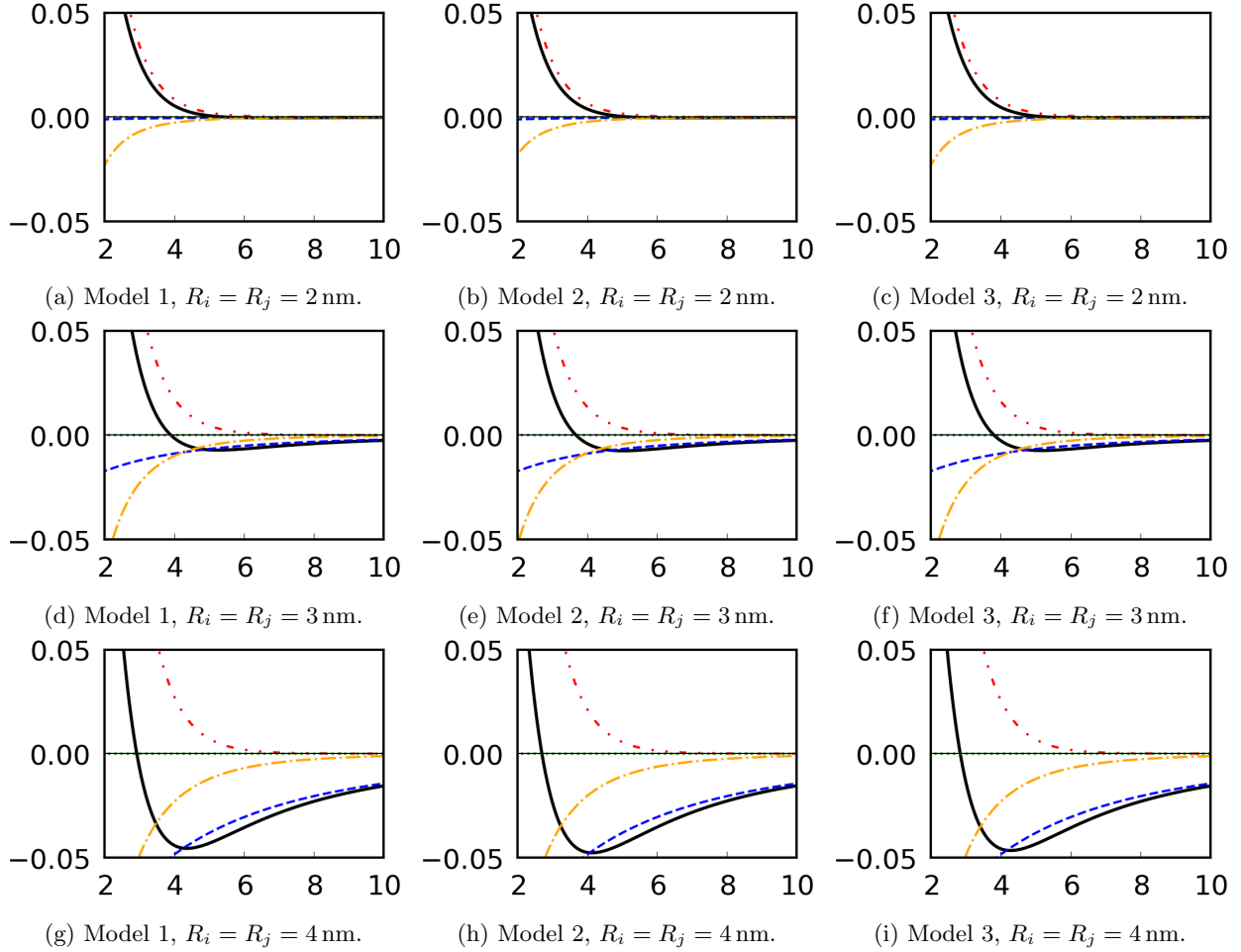


Figure S3: Interaction energy of two nanoparticles with equal radii in dependence on their intersurface distance, in the long range (2 nm to 10 nm), for the models 1, 2 and 3, from left to right. Other nanoparticle parameters are as shown in the article appendices.

Secondary minima

Figure S4 shows heatmaps of the secondary equilibrium positions for some combinations of values for the radii of the interacting particles (R_i and R_j). Wider variations are found in the larger particle rows, which shows that the radius of the smaller particle of the pair has a more determinant role. The differences between the models are not very marked visually, thus we also show some percentual variations between the models' results (Figure S5).

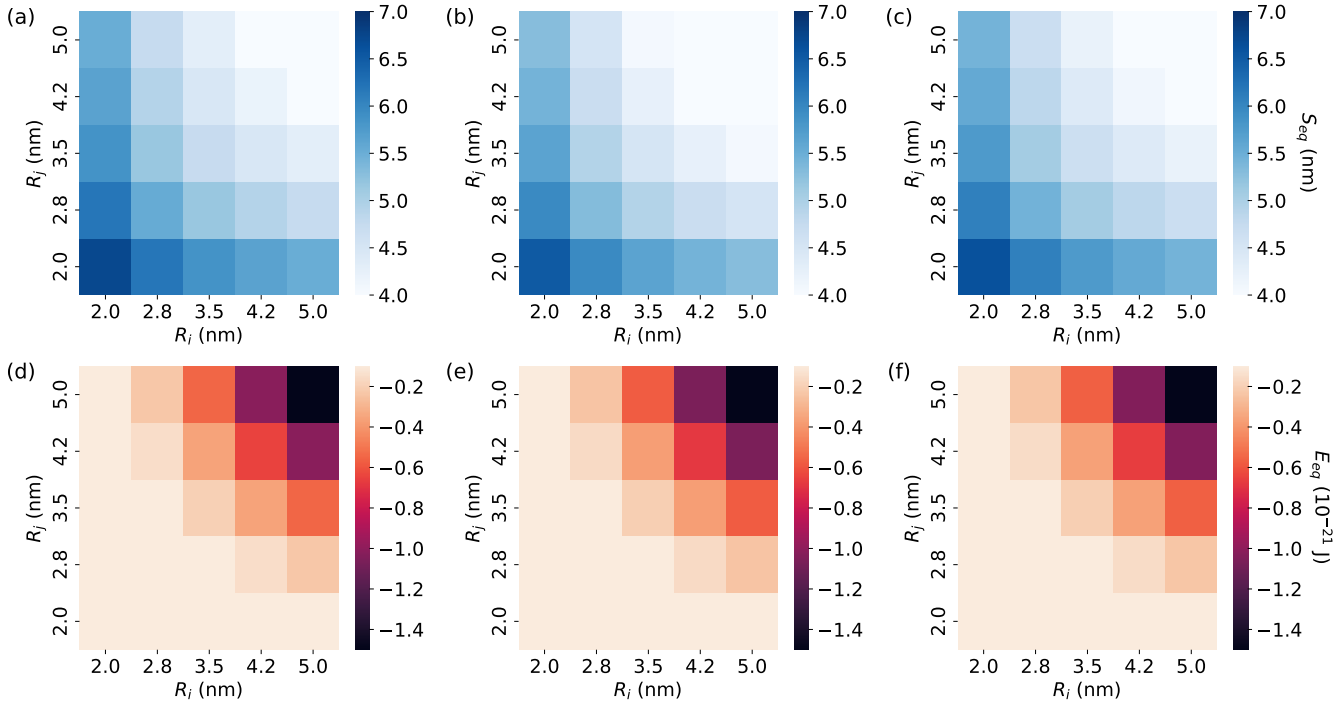


Figure S4: Heatmaps of the secondary equilibrium positions for Models 1 (a), 2 (b), and 3 (c). Below, corresponding heatmaps showing the secondary minima energy for Models 1 (d), 2 (e), and 3 (f) are presented.

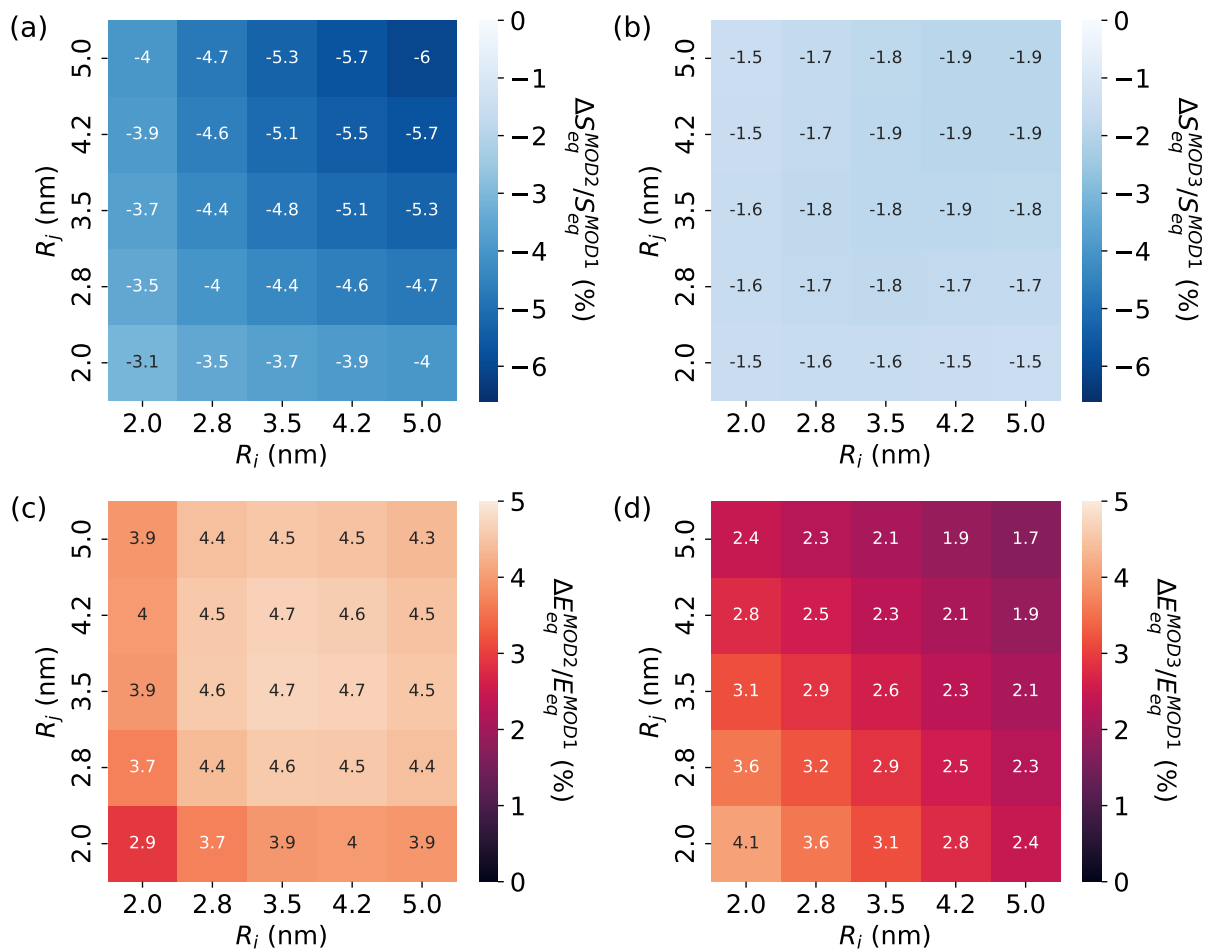


Figure S5: Heatmap showing the percentage difference in the secondary equilibrium distance between Models 2/1 (a) and Models 3/1 (b). The percentage difference in the corresponding energy depth is presented for Models 2/1 (c) and Models 3/1 (d).